

PHOTONICS Research

Cylindrical vector beam revealing multipolar nonlinear scattering for superlocalization of silicon nanostructures

BIN WANG,^{1,2,†} YING CHE,^{2,†} XIANGCHAO ZHONG,² WEN YAN,² TIANYUE ZHANG,^{2,4}  KAI CHEN,²  YI XU,³ 
XIAOXUAN XU,¹ AND XIANGPING LI^{2,5}

¹The Key Laboratory of Weak-Light Nonlinear Photonics, Ministry of Education, School of Physics, Nankai University, Tianjin 300071, China

²Guangdong Provincial Key Laboratory of Optical Fiber Sensing and Communications, Institute of Photonics Technology, Jinan University, Guangzhou 510632, China

³Department of Electronic Engineering, College of Information Science and Technology, Jinan University, Guangzhou 510632, China

⁴e-mail: tyzhang@jnu.edu.cn

⁵e-mail: xiangpingli@jnu.edu.cn

Received 8 January 2021; revised 9 March 2021; accepted 10 March 2021; posted 25 March 2021 (Doc. ID 419300); published 20 May 2021

The resonant optical excitation of dielectric nanostructures offers unique opportunities for developing remarkable nanophotonic devices. Light that is structured by tailoring the vectorial characteristics of the light beam provides an additional degree of freedom in achieving flexible control of multipolar resonances at the nanoscale. Here, we investigate the nonlinear scattering of subwavelength silicon (Si) nanostructures with radially and azimuthally polarized cylindrical vector beams to show a strong dependence of the photothermal nonlinearity on the polarization state of the applied light. The resonant magnetic dipole, selectively excited by an azimuthally polarized beam, enables enhanced photothermal nonlinearity, thereby inducing large scattering saturation. In contrast, radially polarized beam illumination shows no observable nonlinearity owing to off-resonance excitation. Numerical analysis reveals a difference of more than 2 orders of magnitude in photothermal nonlinearity under two types of polarization excitations. Nonlinear scattering and the unique doughnut-shaped focal spot generated by the azimuthally polarized beam are demonstrated as enabling far-field high-resolution localization of nanostructured Si with an accuracy approaching 50 nm. Our study extends the horizons of active Si photonics and holds great potential for label-free superresolution imaging of Si nanostructures. © 2021 Chinese Laser Press

<https://doi.org/10.1364/PRJ.419300>

1. INTRODUCTION

Dielectric nanomaterials with high refractive indices have been widely studied in recent years owing to their low optical loss, unique optical responses, and compatibility with the manufacturing process of complementary metal-oxide semiconductor technology [1–3]. Strong electric and magnetic Mie resonances in high-index dielectric nanostructures play a crucial role in the nanoscale confinement of electromagnetic near fields for the enhancement of many optical nonlinear effects [4–7]. In addition, they engender various interference phenomena in the far field by engineering the interplay of optical-induced multipoles [8,9]. New developments further reveal that, even though the ohmic losses are inherently low for dielectrics, Mie resonances provide strong local heat on account of the absorption of incident light and the transduction into thermal energy. These attributes substantially increase the temperature of nanostructures, paving the way for all-dielectric thermophotonics [10–12]. Isolated resonant dielectric nanoparticles have been

identified as highly effective optical heaters [10,13–15]. Moreover, functional all-dielectric metasurfaces can be actively tuned simply through thermal actuations based on the large thermo-optical coefficient of the materials [16–21]. Giant photothermal nonlinearity mediated by resonant modes has been recently revealed in a single silicon (Si) nanostructure, which can be 3 to 4 orders of magnitude greater than unstructured bulk Si [22,23]. Such a unique photothermal mechanism provides a novel scenario of dynamical reversible tuning of optical responses in all-dielectric nanostructures through an optical stimulus.

The significant advantage of all-optical tuning is that unprecedented flexibility in manipulating multipolar light-matter interactions can be facilitated by means of smart engineering of the illumination beam [24–26]. By harnessing spatially variant electric polarizations mediated by tightly focused cylindrical vector beams (CVBs), different multipolar resonances can be selectively excited, resulting in separate control over the induced electric and magnetic multipoles [27–29].

Fully exploiting these benefits enables the extreme tailoring of both linear and nonlinear emission properties. The excitation of dark modes [30,31], angular tuning of directional scattering [32–34], and enhanced nonlinear light generation [35–38] in all-dielectric nanostructures have been increasingly observed. In particular, the unique focusing properties drive the recently developed concepts of vector-field nonlinear microscopy by utilizing CVBs for the characterization of nanostructures [36,39], thereby expanding the capabilities of nonlinear microscopes. Owing to these developments, exciting advances are expected to reveal new applications that leverage innovative combinations of high-index metaoptics and vector-field nonlinear microscopy.

In this report, we show the photothermal nonlinearity of Si nanoresonators that are strongly influenced by excitation polarization states. Resonance-enhanced photothermal nonlinearity governed by an out-of-plane magnetic dipole (MD) is achieved via azimuthally polarized (AP) beam illumination with the desired excitation wavelength, which is 80% reversible, as well as by repeatable all-optical modulation of the scattering signal. In contrast, a significantly low photothermal nonlinearity is observed in Si nanodisks pumped with a radially polarized (RP) beam, which results from differently induced multipolar modes. Remarkable scattering saturation, which is a consequence of the intense AP beam, efficiently suppresses the scattering intensity of the overlapping excitation of the probe beam. This naturally constitutes a configuration similar to the stimulated emission depletion (STED) microscope [40,41]. In our technique, the AP beam generates a doughnut focal spot and is used as a robust saturation beam. The beam is scattered from Si nanodisks under the Gaussian probe beam to engender an imaging contrast. We therefore demonstrate the realization of far-field high-resolution localization of densely spaced Si nanodisk arrays with exceptional localization accuracy up to 50 nm ($\lambda/11$). Our results provide a new means of controlling and modulating the nonlinear scattering response induced by the photothermal mechanism. Moreover, our proposed technique offers important potential in applications in label-free high-resolution imaging for all-dielectric metasurfaces and Si photonics.

2. RESULTS AND DISCUSSION

The principle of our proposed approach is schematically illustrated in Fig. 1(a). Si nanodisks are illuminated by a tightly focused AP saturation beam and a Gaussian probe beam. The Si nanodisks on the glass substrate were fabricated by colloidal-mask lithography followed by coupled plasma reactive ion etching [23]. The morphologies of the prepared samples were characterized by scanning electron microscopy (SEM) and atomic force microscopy (AFM) (Figs. 5 and 6 in Appendix A). As shown in the Fig. 1(a), the designed nanodisks support a strong MD resonance at the optical pump wavelength (continuous wave, 639 nm). When illuminated by a 639 nm AP beam with increased intensities, the Si nanodisks are subjected to a nonlinear scattering process owing to the MD resonant-enhanced photothermal effect [22,23]. This leads to efficient suppression of the scattering signal of the probe beam (561 nm). The created all-optical switch with overlapping excitation of dual beams provides the basis for superresolution imaging of Si, similar to the sharp point spread function (PSF) achieved in the STED principle.

A schematic of the experimental setup for measuring nonlinear scattering signals from Si nanodisks and realization of superlocalization imaging is shown in Fig. 1(b). A commercial polarization converter (ARCOptix, S.A.) was used to convert a linearly polarized (LP) continuous wave laser beam of 639 nm collimated by a 4f system into an AP beam. The verification of the polarization state of AP is shown by Fig. 7 in Appendix A. It was then collinearly aligned with the LP Gaussian mode probe beam (561 nm). The two laser beams were simultaneously scanned through the Si nanodisks, and the backward scattering of the sample was collected using an oil-immersed objective lens (100 \times , NA = 1.4, Olympus). The microscope scattering images were obtained by synchronizing a photomultiplier tube (PMT) and a galvo mirror scanner. They were recorded with a step size of 7 nm and a dwell time of 10 μ s.

Numerical simulations were first performed to analyze the induced multipoles within a single Si nanodisk by tightly focused CVBs. Multipolar decomposition of the total scattering spectra [23] was used to identify the contributing modes. As observed in Fig. 2, the scattering spectra of the nanodisks

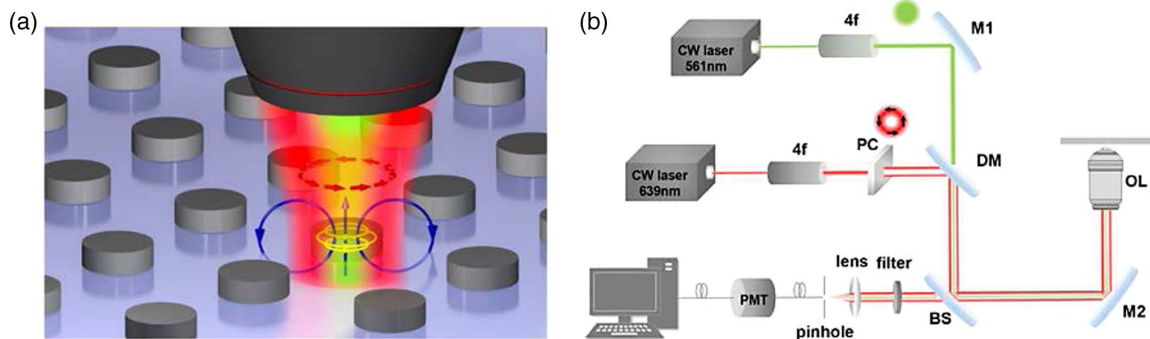


Fig. 1. Schematic illustration of the superlocalization imaging and experimental setup. (a) The principle of superlocalization imaging is based on scattering suppression of Si nanodisks at the peripherals of the doughnut-shaped AP saturation beam. (b) Diagram of the reflectance laser scanning confocal system. M1, M2, silver mirrors; DM, dichroic mirror; BS, beam splitter; OL, objective lens; PC, polarization converter.

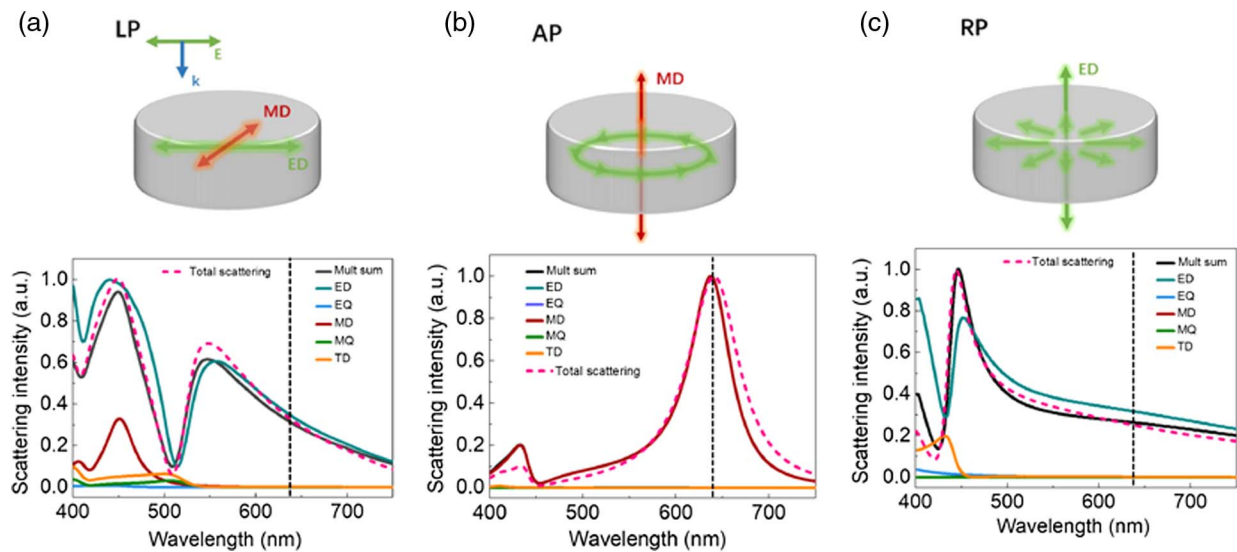


Fig. 2. Simulated total scattering spectra and the Cartesian multipolar decomposition of single Si nanodisks (diameter $D = 200$ nm, height $h = 50$ nm) under (a) linear and (b),(c) CVB illumination. Black dashed lines indicate the position of excitation wavelength.

illuminated by the AP or RP beams noticeably differ from those acquired by LP excitation. Both electric and magnetic multipole resonances are accessible by LP excitation. In contrast, the AP beam contains purely transverse fields at the beam focus, which excites the magnetic Mie resonances with the dominant contribution from the out-of-plane MD mode [Fig. 2(b)]. Conversely, the RP beam has a strong longitudinal electric field component, resulting in the generation of a longitudinal electric dipole (ED) as well as a toroidal dipole (TD). Notably, with the rationally designed dimensions of the Si nanodisks in the present study, the MD mode excited by the AP beam has well-tuned resonance with the excitation wavelength. The LP and RP beams with the same wavelength are much less efficient in coupling to the nanodisks for excitation at the ED resonance tail. Therefore, the largest photothermal nonlinearity can be expected by means of efficient excitation utilizing AP illumination.

Based on the above findings, we experimentally examined the photothermal nonlinearity by measuring the backward scattering from the Si nanodisks at increased excitation intensities (see discussions in Appendix A.3 about the total scattering and the backward scattering). The Si nanodisks converted AP excitation light into internal heat through the MD resonantly enhanced optical absorption, which substantially raised the nanodisk temperature. The temperature increase then affected the refractive index as well as the scattering cross section, thus leading to nonlinear optical scattering. This Mie-resonance-enhanced photothermal effect was validated by our simulation results. The simulated scattering cross section (C_{sca}) is plotted in Appendix A, Fig. 8 to show the spectral response and the tuning of the Mie resonances in accordance with the temperature increments. The irradiance-induced temperature rise leads to large redshifting of the Mie resonances. Furthermore, the C_{sca} associated with the excitation wavelength can be dramatically varied, yielding 70% suppression, which consequently leads to scattering saturation. The PSFs in the

scattering images display distinctive features when scattering begins to saturate, as shown in Figs. 3(a)–3(c). Conceptually, considering a focus with a doughnut profile, saturation should start from the periphery, where the intensity is strongest, to induce saturation. As a result, the variations of the PSF are experimentally observed, manifesting the evolution of nonlinear scattering.

Figure 3(d) shows that nonlinear scattering can empower distinctive PSFs in confocal reflectance imaging of closely packed Si nanodisk arrays. The confocal image at low excitation intensities for such nanodisk arrays is blurry, owing to the restriction of the diffraction limit. However, scattering saturation at high excitation intensities leads to a large reduction in scattering, thus producing subdiffraction features in scattering PSFs. For comparison, scattering images were also recorded under the illumination of the RP beams. An RP beam with the same wavelength turns off the MD resonance, exciting only electric modes. At a wavelength of 639 nm, the RP beam excites at the spectral position far from the ED peak, producing negligible photothermal nonlinearity. Therefore, only a linear scattering behavior is observed [Fig. 3(e)]. Numerical calculations reveal that there are more than 2 orders of magnitude difference when changing the excitation beam from AP to RP (Fig. 8 in Appendix A). It is also worth noting that strong nonlinearity is also expected in the anapole state, where a TD and an ED are coexcited. Nevertheless, anapole excitation in the Si nanodisks falls outside the experimentally accessible range.

By combining the advantages of photothermal nonlinear scattering and the unique focusing property enabled by the AP beam, we demonstrate the far-field localization of nanostructured Si with exceptionally high accuracy (Fig. 4). Previous studies have reported how saturation can be adopted to enhance the optical resolution by controlling the saturation beam intensity to modulate the collinear probe beam light signal [42–45], similar to the STED configuration. Generally, in these STED-like techniques, a circularly polarized vortex beam

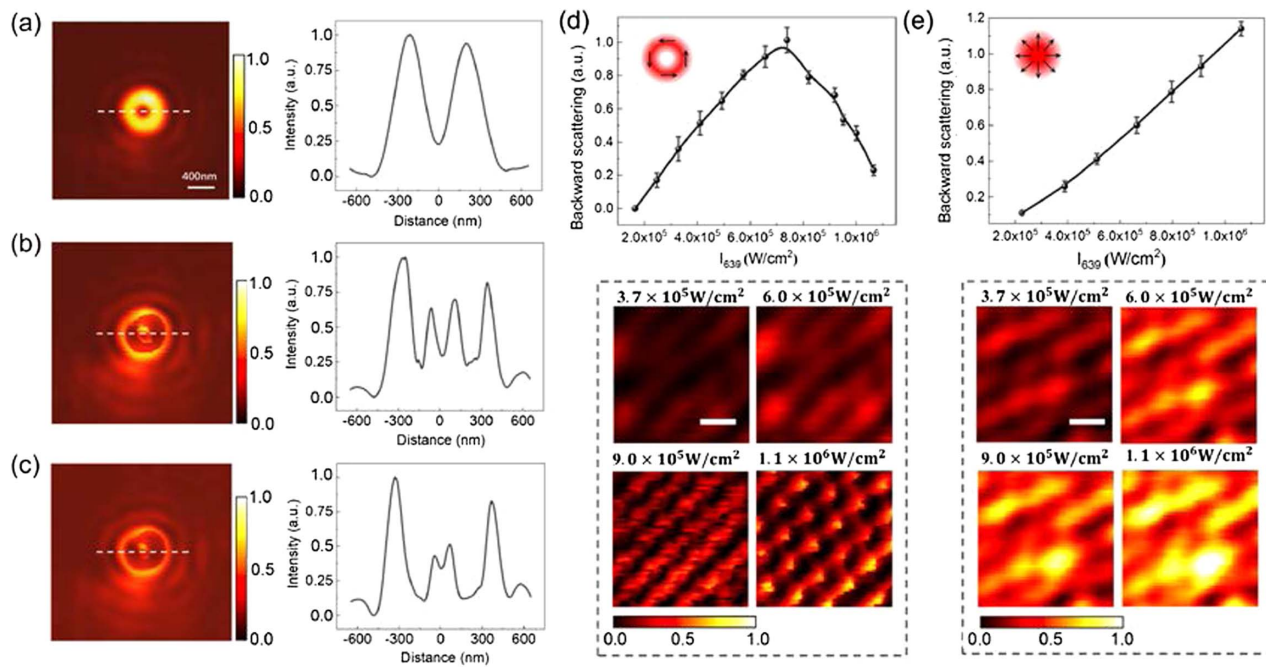


Fig. 3. Experimental observation of photothermal nonlinearity via backward scattering measurements using CVBs. (a)–(c) Measured PSFs of a single nanostructure under different AP beam intensities at a 639 nm wavelength. (a) At low excitation intensity, the PSF shows the doughnut-shaped focal spot generated from the conventional AP. (b),(c) When the intensity reaches a nonlinear region, scattering saturation occurs, and the corresponding PSFs show a low intensity at the doughnut crest. The intensity lateral profiles (white dashed lines) are plotted on the right. (d) The nonlinear dependency of scattering on irradiance intensities and the evolution of PSFs of the Si nanodisk array for AP excitations at a 639 nm wavelength; (e) for RP excitation, negligible nonlinearity is observed, and the scattering shows a linear response in accordance with the increasing irradiance intensities.

is commonly used for generating a doughnut focal spot with zero central intensity. In our present study, a focused AP beam with a high NA objective lens can generate a high-quality doughnut focal spot (Fig. 9 in Appendix A). Moreover, it can be resonantly coupled to the out-of-plane MD mode to induce photothermal nonlinearity, which implicitly fulfills the need for superresolution imaging.

Figure 4(a) presents a series of scattering images with significantly improved resolution under increased saturation beam intensities. These raw superresolved images, combined with the verification of the correlated SEM image, clearly demonstrate that Si nanodisks—indistinguishable in conventional confocal imaging at low excitation intensities—are distinctly resolved at high irradiance intensities (see Visualization 1 for more results). Figure 4(b) quantifies the dependence of localization accuracy on the applied saturation beam intensity, which is based on the statistics of the full width at half-maximum (FWHM) of the imaging spots. The measured FWHM can be sharply squeezed to approximately 50 nm by impinging the AP beam with an intensity of 1.1 MW/cm^2 on the nanodisks to match the MD resonances. Compared to conventional STED fluorescence microscopy [46], our technique reduces the saturation intensity by approximately 2 to 3 orders of magnitude. Moreover, this localization accuracy is the highest achieved to date in accordance with the far-field fluorescence-free scheme. Furthermore, the label-free modality is extremely beneficial for contactless inspection of Si photonics. The reversibility of nonlinear scattering is proved by the complete

recovery of the FWHM of the nanodisks under repeated measurements of switching the saturation beam on and off, as shown in Fig. 4(c), thus confirming the high stability of the entire process.

It should be emphasized that we use Si nanodisks for the proof-of-concept, demonstrating the high-resolution localization based on the photothermal mechanism. The photothermal nonlinearity is associated with the size or shape of the Si nanostructure. Specifically, on one hand, the Si nanostructure illuminated by the laser beam converts incident light into heat. The particle temperature subsequently rises nonlinearly with the incoming light intensity, with the slope that depends on the particle size, shape, laser wavelength, and material properties [22,23]. On the other hand, the size and shape also determine the spectral features of the Mie resonances supported by the structure. Resonant optical excitation enables the boosted photothermal nonlinearity to induce a significant change of permittivity of the nanostructure, resulting in the nonlinear dependence of optical scattering on the illumination intensity. Particularly, the scattering signal decreases when the excitation intensity increases, referred to as scattering saturation. The large scattering saturation produced by photothermal nonlinearity can be utilized as an all-optical control over scattering efficiency of another laser beam, laying the foundation for the high-resolution localization based on STED-inspired imaging techniques. As observed in this work, a deep scattering saturation is highly desirable for higher spatial localization accuracy.

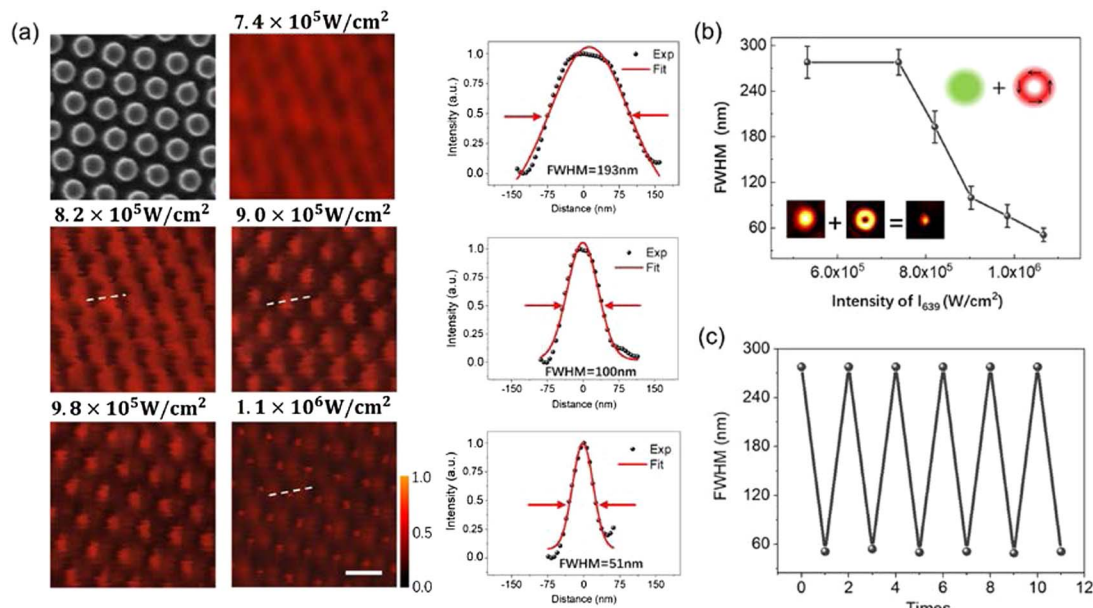


Fig. 4. Superlocalization of densely spaced Si nanodisks. (a) PSFs of nonlinear scattering from periodic Si nanodisk arrays evolving with increasing excitation intensities. A correlated SEM image is also presented. (b) Localization accuracy scaling as PSFs obtained at different saturation AP beam intensities. The error bars represent the deviations of FWHM values from 28 nanodisks in the scanning frame. (c) Reversibility of nonlinear scattering is confirmed by the full recovery of measured FWHM from the same nanodisks under repetitive measurements.

Since the photothermal effect and temperature-dependent permittivity are clearly inherent material properties, the proposed concept is generally applicable to wide nanophotonic systems, especially for dielectric resonant nanostructures made of Si, germanium, III–V semiconductors, or other multi-component materials demonstrating unique Mie resonances. Besides, vectorial light with unique polarization characteristics enables selective and enhanced coupling to multipolar resonances. Therefore, we envision the applicability of our method is universal for other complex vectorial beams to tailor the dominant multipolar resonances, providing flexible control of multipolar resonances at the nanoscale.

3. CONCLUSIONS

In summary, CVBs were implemented to investigate the photothermal nonlinearity of Si nanostructures. Efficient nonlinear scattering was observed by selectively exciting the out-of-plane magnetic Mie resonances with an AP vector beam. Switching to the RP beam resulted in negligible scattering nonlinearity owing to the off-resonance excitation of activated electric multipolar modes. The AP beam with sufficiently high intensities could induce strong scattering saturation of the Si nanodisks on account of the MD-enhanced photothermal effect. An 80% reduction in the scattering signal indicated that the AP beam acted as a saturation beam to efficiently suppress the scattering of another probe beam. In addition, the doughnut-shaped focal spot made the AP beam an ideal candidate for effective STED-like configurations. We further demonstrated the far-field superlocalization of densely packed Si nanodisk arrays with a record-high 50 nm FWHM, corresponding to $\lambda/11$ precision. Considering the compatibility of Si materials and complementary metal-oxide-semiconductor manufacturing

processes, our findings open new possibilities for all-optical label-free inspection of Si-based structures, with great potential for many applications, such as nonlinear nanophotonics, wafer lithography, and Si-integrated circuits.

APPENDIX A

1. Characterizations of Periodic Si Nanodisk Arrays

The morphology of the dense arrays of Si nanodisks was characterized by SEM and AFM. The SEM images in Fig. 5 demonstrate that the prepared Si nanodisks have a smooth surface and large-scale uniformity. The enlarged image shows that the diameter of the Si nanodisks is predominantly 200 nm. Figure 6 shows that the heights of the Si nanodisks are 50 nm.

2. Inspection of Polarization Characteristics of RP Light and AP Light

The beam spot shapes captured by the CCD are presented in the figures below. The polarization state was detected by inserting the analyzer in front of the detector at different angles,

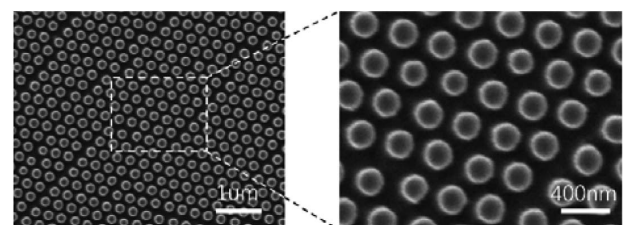


Fig. 5. SEM image and magnified image of Si nanodisk arrays with a diameter of 200 nm and height of 50 nm. Scale bar, 1 μm ; 400 nm.

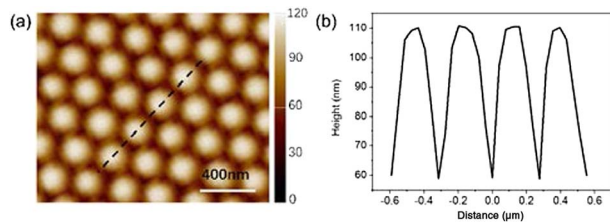


Fig. 6. (a) AFM characterization of the Si nanodisk array sample. Scale bar, 400 nm. (b) Cross section of the height of the nanodisk at the position of the black dotted line.

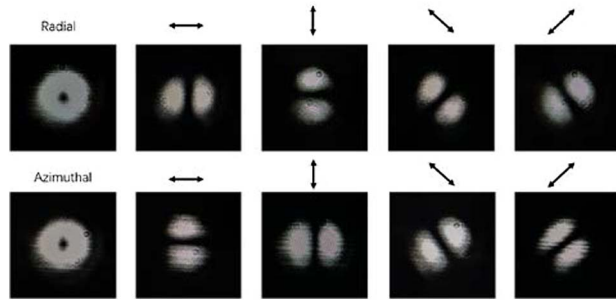


Fig. 7. Experimentally generated radial beam (upper row), azimuthal beam (lower row), and their linear orthogonal components. The black arrows indicate the position of the analyzer.

as shown by the black arrow in Fig. 7. A series of images effectively display the polarization characteristics of the excitation light used.

3. Photothermally Induced Nonlinear Scattering of Si Nanodisks under AP and RP Beams

The photothermal nonlinearity was calculated for Si nanodisks with a diameter of 200 nm and a height of 50 nm. The simulated scattering cross section (C_{sca}) plotted in Fig. 8(a) shows the spectral response and the tuning range of Mie resonances in accordance with temperature increments. Under AP illumination, the irradiance-induced temperature increase from room temperature (RT) to 850°C enables suppression of the normalized C_{sca} from 1 to 0.3, corresponding to 70% modulation [Fig. 8(b)]. This roughly agrees qualitatively with the experimental observation of 80% suppression of the normalized cross section from linear to saturation in Fig. 3(d).

Such a large modulation depth is attributed to the fact that the excitation laser delicately operates in the vicinity of the MD mode. Taking advantage of the resonantly enhanced near-field absorption at the MD excitation causes the Si nanodisks to be rapidly heated. The temperature increase of the nanostructures changes the refractive index of the material, which further alters the light scattering. The temperature growth inside the Si nanodisk can be estimated by the equation $\Delta T = \sigma_{abs} I / 4\pi R_{eq} \kappa \beta$, where κ is the thermal conductivity of the surrounding medium. Considering Si nanodisks on the glass substrate and immersed in the oil environment, κ was taken to be 0.38. $\beta = 1.15$ is a dimensionless geometrical correction factor. R_{eq} denotes the equivalent radius, corresponding to the radius of a sphere with the same volume as the nanodisk. Temperature-dependent optical absorption σ_{abs} is taken into account, and the final laser-induced temperature rise on the excitation intensity is obtained by iterative calculations. This is indicated in Fig. 8(c), with more than 2 orders of magnitude

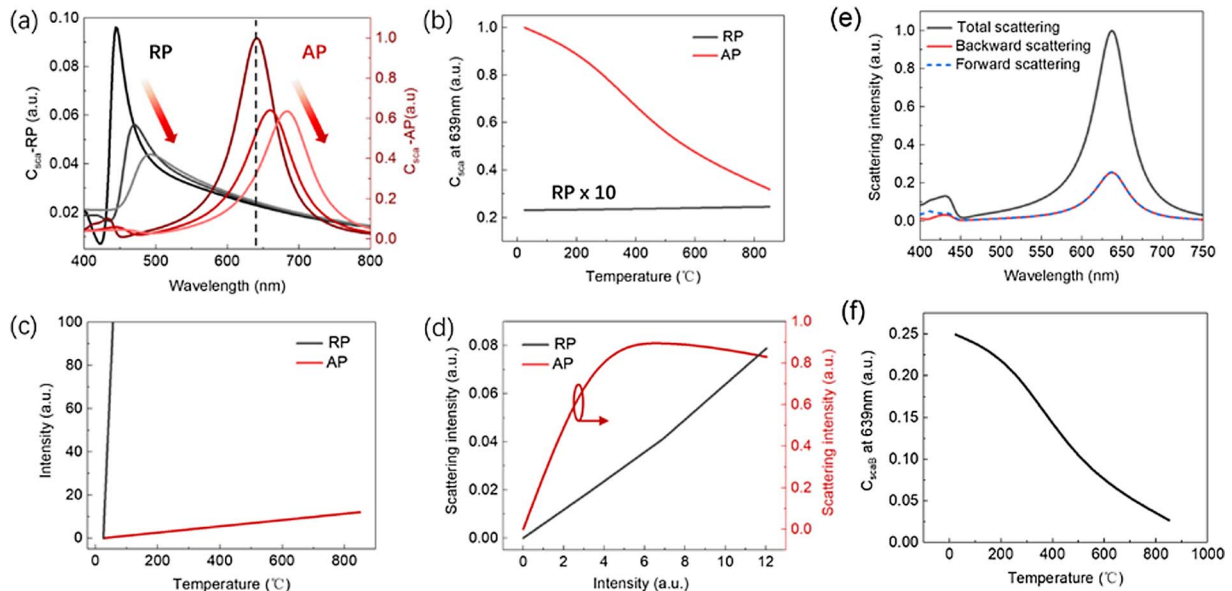


Fig. 8. (a) Photothermal tuning of normalized scattering spectra of Si nanodisks of different polarization states at three representative temperatures: RT, 500°C, and 850°C. The dashed line indicates the position of excitation. (b) Evolution of C_{sca} with increasing temperatures at the excitation wavelength of 639 nm; (c) required excitation intensities for temperature increase of the Si nanodisks under AP and RP illuminations; (d) resulting simulated nonlinear scattering behaviors under AP and RP illuminations; (e) simulated scattering cross sections for total scattering, forward scattering, and backscattering illuminated by AP excitation; (f) evolution of backscattering C_{scaB} with increasing temperatures at the excitation wavelength of 639 nm.

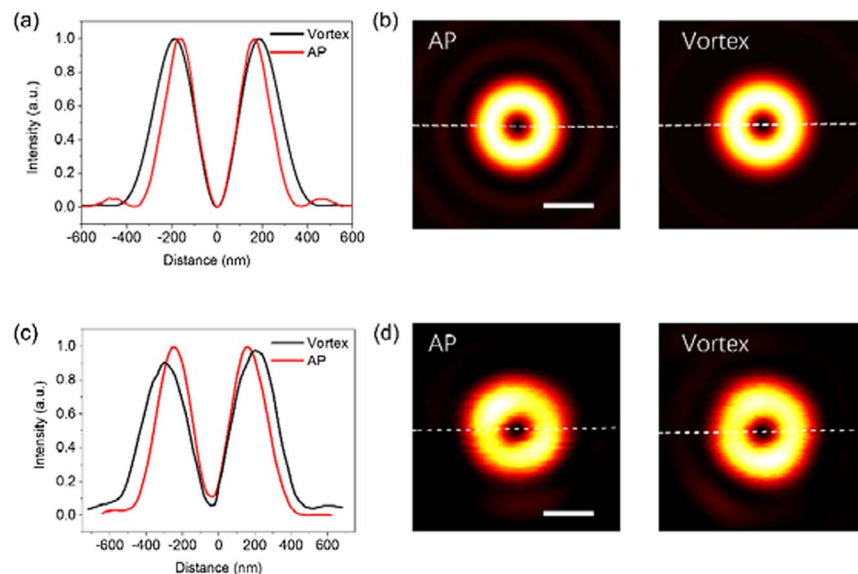


Fig. 9. Comparison of AP beam spot and doughnut-shaped circularly polarized beam spot. (a) The theoretic cross sections at the position of the white dashed lines in (b) are obtained with a laser of 639 nm. Scale bar, 400 nm. (c) The experimental cross sections at the location of the white dotted lines in (d) are obtained by scanning the Si with a diameter of 200 nm with a laser of 639 nm. Scale bar, 400 nm.

difference in photothermal efficiency between the Si nanodisks under AP and RP excitations.

For the simulation of the scattering spectra and the Cartesian multipolar decomposition in Fig. 2, box monitors were used that collected all the scattering fields of 4π solid angles. On the other hand, the measured scattering in experiments is the backscattered light collected from the objective with a finite NA. To resolve this problem, we perform the calculations of scattering spectra accounting total scattering, forward scattering, and backward scattering. It should be noted that in the calculations of backward scattering C_{scaB} in Figs. 8(e) and 8(f), a plane monitor was employed. The plane monitor was positioned at 400 nm from the simulation center, with a monitor size of 1900 nm by 1900 nm, based on the consideration of matching the maximum collection angle of the objective lens (NA = 1.4) used in our experiments.

As can be seen in Fig. 8, the nanodisk scatters light almost equally in forward and backward directions. And the total and backward scattering cross sections experience large suppression with temperature rise in the same trend, thus indicating the scattering depletion not depending on the collection angle of the objective lens. This also clarifies that our suppression of the scattering originates from the photothermal tuning of MD modes by the AP beam instead of redistribution of forward and backward radiations.

4. Comparison of Doughnut Focal Spots between Right-Handed Circularly Polarized Vortex Beam and AP Beam

An AP beam can yield a doughnut-like spot of uniform intensity. It can generate a smaller focal spot than those generated by the circularly polarized doughnut-like spots produced by the phase plate, as shown in Figs. 9(a) and 9(b). According to the theoretical calculations, the peak distance between the AP spots is 330 nm, which is 48 nm smaller than that between

the vortex spots. The distance of peaks of the experimental AP spot is 410 nm. However, the vortex spots are with 500 nm, as shown in Figs. 9(c) and 9(d). This finding is consistent with the theoretical conclusion that the AP light spot is smaller than the vortex light spot. The characteristics of the smaller focusing spot under AP polarized excitation light provide a convenient and robust way for STED-like imaging experiments.

Funding. National Key Research and Development Program of China (2018YFB1107200); National Natural Science Foundation of China (61805107); Guangdong Provincial Innovation and Entrepreneurship Project (2016ZT06D081).

Disclosures. The authors declare no conflicts of interest.

[†]These authors contributed equally to this work.

REFERENCES

1. A. I. Kuznetsov, A. E. Miroshnichenko, M. L. Brongersma, Y. S. Kivshar, and B. Luk'yanchuk, "Optically resonant dielectric nanostructures," *Science* **354**, aag2472 (2016).
2. S. Kruk and Y. Kivshar, "Functional meta-optics and nanophotonics governed by Mie resonances," *ACS Photon.* **4**, 2638–2649 (2017).
3. I. Staude and J. Schilling, "Metamaterial-inspired silicon nanophotonics," *Nat. Photonics* **11**, 274–284 (2017).
4. D. Smirnova and Y. S. Kivshar, "Multipolar nonlinear nanophotonics," *Optica* **3**, 1241–1255 (2016).
5. Y. Kivshar, "All-dielectric meta-optics and non-linear nanophotonics," *Natl. Sci. Rev.* **5**, 144–158 (2018).
6. Z. Liu, Y. Xu, Y. Lin, J. Xiang, T. Feng, Q. Cao, J. Li, S. Lan, and J. Liu, "High-Q quasibound states in the continuum for nonlinear metasurfaces," *Phys. Rev. Lett.* **123**, 253901 (2019).
7. C. Zou, J. Sautter, F. Setzpfandt, and I. Staude, "Resonant dielectric metasurfaces: active tuning and nonlinear effects," *J. Phys. Condens. Matter* **52**, 373002 (2019).

8. W. Liu and Y. S. Kivshar, "Multipolar interference effects in nanophotonics," *Philos. Trans. R. Soc. A* **375**, 20160317 (2017).
9. T. Liu, R. Xu, P. Yu, Z. Wang, and J. Takahara, "Multipole and multi-mode engineering in Mie resonance-based metastructures," *Nanophotonics* **9**, 1115–1137 (2020).
10. G. P. Zograf, M. I. Petrov, D. A. Zuev, P. A. Dmitriev, V. A. Milichko, S. V. Makarov, and P. A. Belov, "Resonant nonplasmonic nanoparticles for efficient temperature-feedback optical heating," *Nano Lett.* **17**, 2945–2952 (2017).
11. M. Aouassa, E. Mitsai, S. Syubaev, D. Pavlov, A. Zhizhchenko, I. Jadli, L. Hassayoun, G. Zograf, S. Makarov, and A. Kuchmizhak, "Temperature-feedback direct laser reshaping of silicon nanostructures," *Appl. Phys. Lett.* **111**, 243103 (2017).
12. T. Yatsui, "Recent improvement of silicon absorption in opto-electric devices," *Opto-Electron. Adv.* **2**, 19002301 (2019).
13. Y. Li, X. Yang, Y. Yang, B. Wang, X. Li, and R. Salas-Montiel, "Optical nanoheating of resonant silicon nanoparticles," *Opt. Express* **27**, 30971–30978 (2019).
14. G. P. Zograf, A. S. Timin, A. R. Muslimov, I. I. Shishkin, A. Nominé, J. Ghanbaja, P. Ghosh, Q. Li, M. V. Zyuzin, and S. V. Makarov, "All-optical nanoscale heating and thermometry with resonant dielectric nanoparticles for controllable drug release in living cells," *Laser Photon. Rev.* **14**, 1900082 (2020).
15. J. Yan, Y. Li, Z. Lou, C. Ma, G. Yang, and B. Li, "Active tuning of Mie resonances to realize sensitive photothermal measurement of single nanoparticles," *Mater. Horiz.* **7**, 1542–1551 (2020).
16. M. Rahmani, L. Xu, A. E. Miroshnichenko, A. Komar, R. Camacho-Morales, H. Chen, Y. Zárate, S. Kruk, G. Zhang, D. N. Neshev, and Y. S. Kivshar, "Reversible thermal tuning of all-dielectric metasurfaces," *Adv. Funct. Mater.* **27**, 1700580 (2017).
17. P. P. Iyer, R. A. DeCrescent, T. Lewi, N. Antonellis, and J. A. Schuller, "Uniform thermo-optic tunability of dielectric metalenses," *Phys. Rev. Appl.* **10**, 044029 (2018).
18. T. Lewi, A. B. Nikita, and A. S. Jon, "Thermal tuning capabilities of semiconductor metasurface resonators," *Nanophotonics* **8**, 331–338 (2019).
19. K. Z. Kamali, L. Xu, J. Ward, K. Wang, G. Li, A. E. Miroshnichenko, D. Neshev, and M. Rahmani, "Reversible image contrast manipulation with thermally tunable dielectric metasurfaces," *Nano Micro Small* **15**, 1805142 (2019).
20. M. Bosch, M. R. Shcherbakov, Z. Fan, and G. Shvets, "Polarization states synthesizer based on a thermo-optic dielectric metasurface," *J. Appl. Phys.* **126**, 073102 (2019).
21. J. Berzinš, S. Indrišūnas, S. Fasold, M. Steinert, O. Žukovskaja, D. Cialla-May, P. Gečys, S. M. B. Bäumer, T. Pertsch, and F. Setzpfandt, "Laser-induced spatially-selective tailoring of high-index dielectric metasurfaces," *Opt. Express* **28**, 1539–1553 (2020).
22. Y.-S. Duh, Y. Nagasaki, Y.-L. Tang, P.-H. Wu, H.-Y. Cheng, T.-H. Yen, H.-X. Ding, K. Nishida, I. Hotta, J.-H. Yang, Y.-P. Lo, K.-P. Chen, K. Fujita, C.-W. Chang, K.-H. Lin, J. Takahara, and S.-W. Chu, "Giant photothermal nonlinearity in a single silicon nanostructure," *Nat. Commun.* **11**, 4101 (2020).
23. T. Zhang, Y. Che, K. Chen, J. Xu, Y. Xu, T. Wen, G. Lu, X. Liu, B. Wang, X. Xu, Y.-S. Duh, Y.-L. Tang, J. Han, Y. Cao, B.-O. Guan, S.-W. Chu, and X. Li, "Anapole mediated giant photothermal nonlinearity in nanostructured silicon," *Nat. Commun.* **11**, 3027 (2020).
24. Q. W. Zhan, "Cylindrical vector beams: from mathematical concepts to applications," *Adv. Opt. Photon.* **1**, 1–57 (2009).
25. X. Li, T. H. Lan, C. H. Tien, and M. Gu, "Three-dimensional orientation-unlimited polarization encryption by a single optically configured vectorial beam," *Nat. Commun.* **3**, 998 (2012).
26. M. Xian, Y. Xu, X. Ouyang, Y. Cao, S. Lan, and X. Li, "Segmented cylindrical vector beams for massively-encoded optical data storage," *Sci. Bull.* **65**, 2072–2079 (2020).
27. P. Woźniak, P. Banzer, and G. Leuchs, "Selective switching of individual multipole resonances in single dielectric nanoparticles," *Laser Photon. Rev.* **9**, 231–240 (2015).
28. T. Das, P. P. Iyer, R. A. DeCrescent, and J. A. Schuller, "Beam engineering for selective and enhanced coupling to multipolar resonances," *Phys. Rev. B* **92**, 241110 (2015).
29. J. A. Parker, H. Sugimoto, B. Coe, D. Eggena, M. Fujii, N. F. Scherer, S. K. Gray, and U. Manna, "Excitation of nonradiating anapoles in dielectric nanospheres," *Phys. Rev. Lett.* **124**, 097402 (2020).
30. T. Das and J. A. Schuller, "Dark modes and field enhancements in dielectric dimers illuminated by cylindrical vector beams," *Phys. Rev. B* **95**, 201111 (2017).
31. T.-S. Deng, J. Parker, Y. Yifat, N. Shepherd, and N. F. Scherer, "Dark plasmon modes in symmetric gold nanoparticle dimers illuminated by focused cylindrical vector beams," *J. Phys. Chem. C* **122**, 27662–27672 (2018).
32. M. Neugebauer, P. Wozniak, A. Bag, G. Leuchs, and P. Banzer, "Polarization-controlled directional scattering for nanoscopic position sensing," *Nat. Commun.* **7**, 11286 (2016).
33. Z. Xi, L. Wei, A. J. L. Adam, and H. P. Urbach, "Broadband active tuning of unidirectional scattering from nanoantenna using combined radially and azimuthally polarized beams," *Opt. Lett.* **41**, 33–36 (2016).
34. L. Wei, N. Bhattacharya, and H. P. Urbach, "Adding a spin to Kerker's condition: angular tuning of directional scattering with designed excitation," *Opt. Lett.* **42**, 1776–1779 (2017).
35. E. V. Meik-Gaykazyan, S. S. Kruk, R. Camacho-Morales, L. Xu, M. Rahmani, K. Z. Kamali, A. Lamprianidis, A. E. Miroshnichenko, A. A. Fedyanin, D. N. Neshev, and Y. S. Kivshar, "Selective third-harmonic generation by structured light in Mie-resonant nanoparticles," *ACS Photon.* **5**, 728–733 (2018).
36. R. Camacho-Morales, G. Bautista, X. Zang, L. Xu, L. Turquet, A. Miroshnichenko, H. H. Tan, A. Lamprianidis, M. Rahmani, C. Jagadish, D. N. Neshev, and M. Kauranen, "Resonant harmonic generation in AlGaAs nanoantennas probed by cylindrical vector beams," *Nanoscale* **11**, 1745–1753 (2019).
37. K. Koshelev, S. Kruk, E. Melik-Gaykazyan, J.-H. Choi, A. Bogdanov, H.-G. Park, and Y. Kivshar, "Subwavelength dielectric resonators for nonlinear nanophotonics," *Science* **367**, 288–292 (2020).
38. M. K. Kroychuk, A. S. Shorokhov, D. F. Yagudin, D. A. Shilkin, D. A. Smirnova, I. Volkovskaya, M. R. Shcherbakov, G. Shvets, and A. A. Fedyanin, "Enhanced nonlinear light generation in oligomers of silicon nanoparticles under vector beam illumination," *Nano Lett.* **20**, 3471–3477 (2020).
39. G. Bautista and M. Kauranen, "Vector-field nonlinear microscopy of nanostructures," *ACS Photon.* **3**, 1351–1370 (2016).
40. S. W. Hell and J. Wichmann, "Breaking the diffraction resolution limit by stimulated emission: stimulated-emission-depletion fluorescence microscopy," *Opt. Lett.* **19**, 780–782 (1994).
41. S. W. Hell, "Nanoscopy with focused light," *Ann. Phys.* **527**, 423–445 (2015).
42. P. Wang, M. N. Slipchenko, J. Mitchell, C. Yang, E. O. Potma, X. Xu, and J.-X. Cheng, "Far-field imaging of non-fluorescent species with subdiffraction resolution," *Nat. Photonics* **7**, 449–453 (2013).
43. H. Y. Wu, Y. T. Huang, P. T. Shen, H. Lee, R. Oketani, Y. Yonemaru, M. Yamanaka, S. Shoji, K. H. Lin, C. W. Chang, S. Kawata, K. Fujita, and S. W. Chu, "Ultrasmall all-optical plasmonic switch and its application to superresolution imaging," *Sci. Rep.* **6**, 24293 (2016).
44. J. Xu, T. Zhang, S. Yang, Z. Feng, H. Li, D. Hu, F. Qin, X. Ouyang, Y. Cao, L. Jiang, and X. Li, "Plasmonic nanoprobe for multiplexed fluorescence-free super-resolution imaging," *Adv. Opt. Mater.* **6**, 1800432 (2018).
45. G. Zanini, K. Korobchevskaya, T. Deguchi, A. Diaspro, and P. Bianchini, "Label-free optical nanoscopy of single-layer graphene," *ACS Nano* **13**, 9673–9681 (2019).
46. J. G. Danzl, S. C. Sidenstein, C. Gregor, N. T. Urban, P. Ilgen, S. Jakobs, and S. W. Hell, "Coordinate-targeted fluorescence nanoscopy with multiple off states," *Nat. Photonics* **10**, 12–128 (2016).